



TECHNICAL ARTICLE

Microstructure Evolution in a Cast and Homogenized Nd-Fe-B-Cu Alloy: Experimental Study and Thermodynamic Calculations

SUBHRAJIT PATNAIK ^{1,3}, RANJEET KUMAR,¹ VARINDER PAL,¹
MANAS PALIWAL,^{1,4} MITHUN PALIT,^{2,5} and SUMANTRA MANDAL^{1,6}

1.—Department of Metallurgical and Materials Engineering, Indian Institute of Technology, Kharagpur 721302, India. 2.—Defence Metallurgical Research Laboratory, Kanchanbagh, Hyderabad 500058, India. 3.—e-mail: subhrajit518@iitkgp.ac.in. 4.—e-mail: manas.paliwal@metal.iitkgp.ac.in. 5.—e-mail: mithun@dmrl.drdo.in. 6.—e-mail: sumantra.mandal@metal.iitkgp.ac.in

A commercial grade Nd_{15.5}Fe₇₈B₅Cu_{1.5} alloy was prepared through the melting-casting route. The as-cast (AC) alloy was characterized by X-ray diffraction (XRD) and scanning electron microscopy techniques. XRD and energy-dispersive spectroscopy analyses revealed the presence of Nd₂Fe₁₄B, Nd₂Fe₁₇, Nd-rich phase (Nd/NdCu eutectic), and α -Fe phases in the AC specimen. Retainment of α -Fe in the AC microstructure makes a core-shell type microstructure in this condition. Thermodynamic predictions based on the non-equilibrium (Scheil-Gulliver) solidification calculations validate the retainment of both α -Fe and Nd₂Fe₁₇ phases in the AC microstructure. A homogenization treatment has been conducted at 1373 K for 2 h, which effectively results in a substantial reduction in the phase fraction of remnant α -Fe.

INTRODUCTION

Nd-Fe-B alloys are the candidates for permanent magnets that are extensively used in electronic data storage devices, hybrid electric vehicles, and wind power generators.^{1–3} Based on production methods, the Nd-Fe-B magnets are broadly categorized into three groups: sintered, hot deformed, and bonded magnets.⁴ To attain optimal properties from the Nd-Fe-B magnets, fully dense and textured magnets are preferred akin to the sintered magnets, without the use of any binders, as is the case in bonded magnets.⁵ The state-of-the-art production of the alloy involves a sintering process that is commonly used to produce high performance Nd-Fe-B magnets.⁶ The advanced sintering process used for production of the Nd-Fe-B alloy encompasses a sophisticated multistep powder metallurgy process that begins with melting of alloy ingots, progresses

through powder synthesis, magnetic field alignment, pressing, and culminates in sintering followed by subsequent annealing.⁶ Alternatively, these alloys can also be produced through die upsetting of the precursors prepared through melt spinning, followed by hot compaction,⁷ and spark plasma sintering of powders prepared through powder metallurgy techniques.⁸ Irrespective of the production route, an ideal finished component should comprise a microstructure with individual matrix Nd₂Fe₁₄B crystallites separated by a thin Nd-rich grain boundary layer for obtaining higher coercivity.⁹ Except for the melt spinning process (i.e., rapid solidification route), the microstructure of the starting material employed in producing sintered magnet holds significant importance.¹⁰ In all the instances mentioned for the production of sintered Nd-Fe-B alloy, the multistep powder metallurgical processes outlined above commence with vacuum induction melting and casting process.¹¹ Therefore, a considerable amount of effort is still focused on the studies of solidification behavior and phase transformation related to Nd-Fe-B alloys with

other alloying additions.^{12,13} Under normal cooling rates observed during casting of the Nd-Fe-B ingots, undesirable α -Fe phase is typically observed in the cast microstructure.^{11,14,15} The α -Fe phase is found in the microstructure as a remnant unreacted pro-peritectic phase, which has a debilitating effect on the hard magnetic property of the alloy.^{11,16} Accordingly, to circumvent the significant presence of α -Fe phase in the post-solidification microstructure, usually a rare-earth rich composition is selected to ensure congruent solidification of the hard magnetic Nd₂Fe₁₄B phase directly from the liquid.¹⁷ However, adopting such an approach leads to an increase in the volume fraction of the Nd-rich phase at grain boundaries and triple junction regions, which dilutes the remanence of the final sintered magnet. Alternatively, a post solidification homogenization heat treatment is typically employed on the cast ingots to reduce the amount of α -Fe in the microstructure which improves the prospects of achieving better magnetic properties in the final sintered magnet.^{16,18}

In the present study, an Nd-Fe-B-Cu alloy is prepared through melting and casting, and subsequently a heat treatment is carried out to homogenize the as-cast (AC) microstructure. To understand the solidification sequence during casting of the alloy, Scheil-Gulliver (non-equilibrium solidification model) calculations are performed and compared with the microstructure of the AC alloy. In addition, equilibrium solidification calculations are performed to finalize an appropriate homogenization temperature. The study also investigates the phase evolution and microstructural changes following the post-solidification homogenization heat treatment of the cast Nd-Fe-B-Cu alloy. The thermodynamic calculations, along with experimental validation, assist in understanding the development of microstructure in both AC and as-homogenized (AH) alloys.

EXPERIMENTAL PROCEDURE

In this study, thermodynamic calculations for the Nd-Fe-B-Cu (Nd_{15.5}Fe₇₈B₅Cu_{1.5}) system were performed with FactSage 8.1 thermochemical software.¹⁹ The calculations were carried out using the thermodynamic database of the Nd-Fe-B system developed by Van Ende and Jung.²⁰ In addition, optimized parameters of Cu-Nd,^{21,22} Cu-B,²³ and Cu-Fe²⁴ binaries were added to the existing ternary Nd-Fe-B system. As a result, a comprehensive database was prepared and used to understand the phase equilibria in the investigated quaternary system. Alloy ingots with the composition mentioned in Table I were prepared by vacuum induction melting of high-purity elemental ingredients, *viz.*, Nd (> 99.9% purity), Fe, B, and Cu (> 99.99% purity) under Ar atmosphere. The alloy composition was prepared on a 1000-g scale and at an induction power of 10 kW. An excess of 3% Nd has been added

Table I. Nd-Fe-B-Cu alloy composition (wt.%) employed in this study

Nd	Fe	Cu	B
33.2	64.6	1.4	0.8

to compensate for the loss of Nd owing to oxidation and evaporation. Details regarding the sequence of element addition while melting are reported elsewhere.²⁵ The melt was cast into a mild steel mold and slowly cooled in the furnace under an Ar atmosphere. A pan-cake shaped ingot (thickness = 30 mm, diameter = 70 mm) was obtained. Differential scanning calorimetry (DSC) was carried out on the AC alloy, for which 10–15 mg of powder specimen was taken and heated at 10 K/min in a PerkinElmer Pyris Diamond DTA-TG analyzer. To perform homogenization treatment, a specimen (10 mm × 10 mm × 10 mm) from the AC ingot was sectioned, wrapped with Ta foil, and homogenized at 1373 K for 2 h under an Ar atmosphere in a vacuum tube furnace (Model: RHTC 80-450/15, Nabertherm GmbH, Germany). After homogenization, the specimen was slowly cooled in the furnace under Ar atmosphere. A schematic illustrating the experimental steps carried out along with the processing conditions is shown in Fig. 1.

Microstructural investigations on both AC and AH specimens were carried out using X-ray diffraction (XRD) and field emission scanning electron microscopy (FE-SEM) techniques. The XRD patterns were obtained using a Bruker D8 Advance A25 X-ray diffractometer with a Cu-K_α target at a step size of 0.02° over the 2θ range of 20°–90°. The XRD peaks were identified using X'pert HighScore Plus software and further analyzed with the help of the ICDD PDF-4 + database. For SEM observation, all specimens were ground with SiC paper starting from 320 grit to 4000 grit followed by polishing using 1 μm and 0.25 μm diamond suspension. The polished specimens were etched with 2% Nital solution. The SEM micrographs and energy dispersive X-ray spectroscopy (EDS) data were acquired in backscattered electron (BSE) imaging mode using a ZEISS MERLIN microscope operated at an acceleration voltage of 15 kV.

RESULTS AND DISCUSSION

XRD Analysis

The XRD analysis of the AC alloy, shown in Fig. 2, reveals peaks corresponding to Nd₂Fe₁₄B, α -Fe, α -Nd, and NdCu phase. ICDD PDF numbers #04-006-3648, #04-007-9753, and #01-078-6511 are used as references for identification of Nd₂Fe₁₄B, α -Fe, and NdCu phase, respectively. In addition, the XRD pattern provided by Siva Kumar et al.²⁶ is used as reference for the α -Nd phase. The peaks of the NdCu

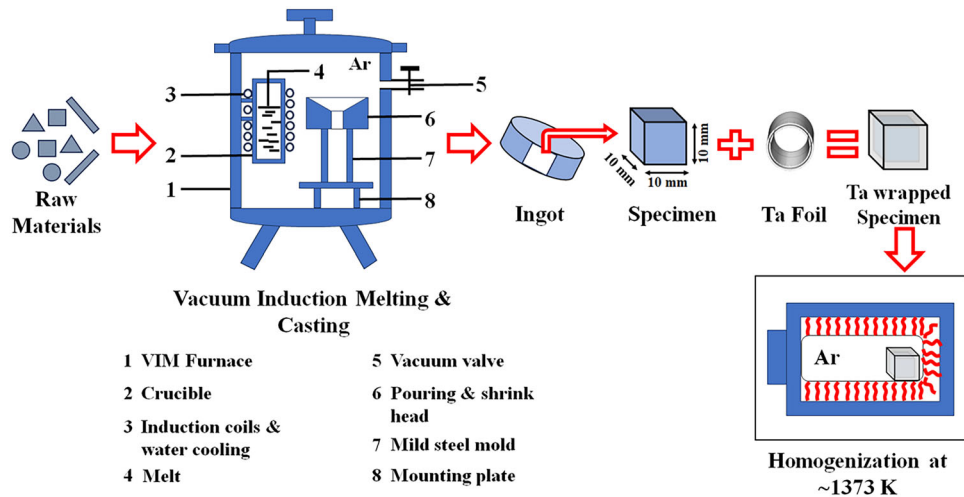


Fig. 1. Schematic showing the experimental steps adopted in this work.

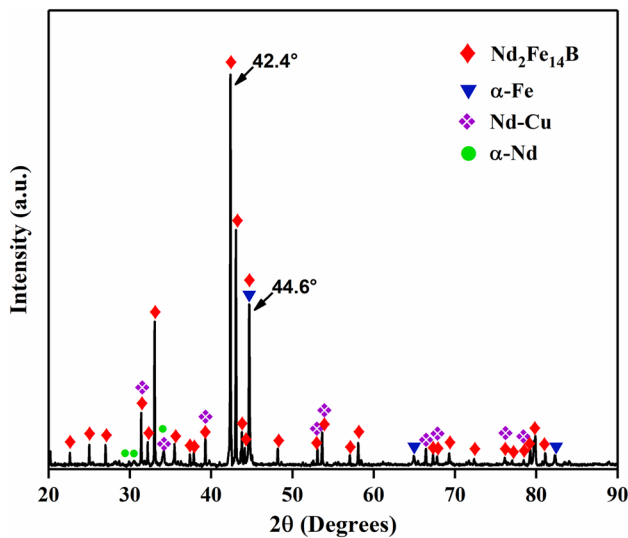


Fig. 2. XRD pattern of the AC alloy.

phase exhibit considerable overlap with those of $\text{Nd}_2\text{Fe}_{14}\text{B}$ phase at most of the 2θ positions. The XRD analysis indicates that the peak positions of $\alpha\text{-Fe}$ and $\text{Nd}_2\text{Fe}_{14}\text{B}$ phases coincide with each other at 2θ value of 44.6° . The peak with the highest intensity is observed at 2θ value of 42.4° , which corresponds to the $\text{Nd}_2\text{Fe}_{14}\text{B}$ phase.

Microstructure and Thermodynamic Correlation

In Fig. 3a, the BSE micrograph of the AC specimen reveals four different Z (atomic number) contrasts: light gray, dark gray, dark, and bright regions, as indicated with red, blue, yellow, and green arrows, respectively. Figure 3b, c and d depicts the elemental distribution maps for Fe, Nd, and Cu, corresponding to the BSE micrograph in Fig. 3a. Clearly, the dark region (indicated by yellow arrows in Fig. 3a) is abundant in Fe, whereas

the bright region (indicated with green arrows in Fig. 3a) is enriched in Nd and Cu. On the other hand, no appreciable difference in Z-contrast is discerned between the light gray and dark gray regions through the elemental distribution map. The corresponding point EDS results of the light gray (marked by red circle in Fig. 3a) and dark gray (marked by blue circle in Fig. 3a) regions are shown in Fig. 3e and f, respectively. The stoichiometric ratio obtained from the EDS analyses indicate that the light gray region is $\text{Nd}_2\text{Fe}_{14}\text{B}$, whereas the dark gray region is $\text{Nd}_2\text{Fe}_{17}$. Results from XRD patterns (Fig. 2) and EDS elemental maps (Fig. 3b, c and d) suggest that dark (marked by yellow arrow in Fig. 3a) and bright (marked by green arrow in Fig. 3a) regions in Fig. 3a correspond to $\alpha\text{-Fe}$ and Nd-rich phases, respectively. A high magnification BSE image highlighting the Nd-rich phase is shown in Fig. 3g and the elemental distribution results are represented in Fig. 3h and i. A combined observation from the XRD pattern in Fig. 2 and the elemental distribution results in Fig. 3h and i suggests that the Nd-rich inter-dendritic region consists of a eutectic mixture of $\alpha\text{-Nd}$ and NdCu phases. The average phase fraction values corresponding to the phases investigated in the BSE microstructure are calculated with the help of ImageJ software and the results are represented in Table II. Although traces of $\text{Nd}_2\text{Fe}_{17}$ phase are observed in the AC microstructure, XRD peaks for the same are not evident in Fig. 2 because of its limited presence in the microstructure. Evidently, analysis of the phase fraction values suggests that the $\text{Nd}_2\text{Fe}_{14}\text{B}$ constitutes the major phase in the AC microstructure.

The equilibrium phase formation in the alloy system as a function of temperature is shown in Fig. 4a. The equilibrium cooling plot shows that $\gamma\text{-Fe}$ is the primary phase forming as the solidification begins at ~ 1560 K. Upon further cooling, the amount of $\gamma\text{-Fe}$ increases up to 30 wt.% and then

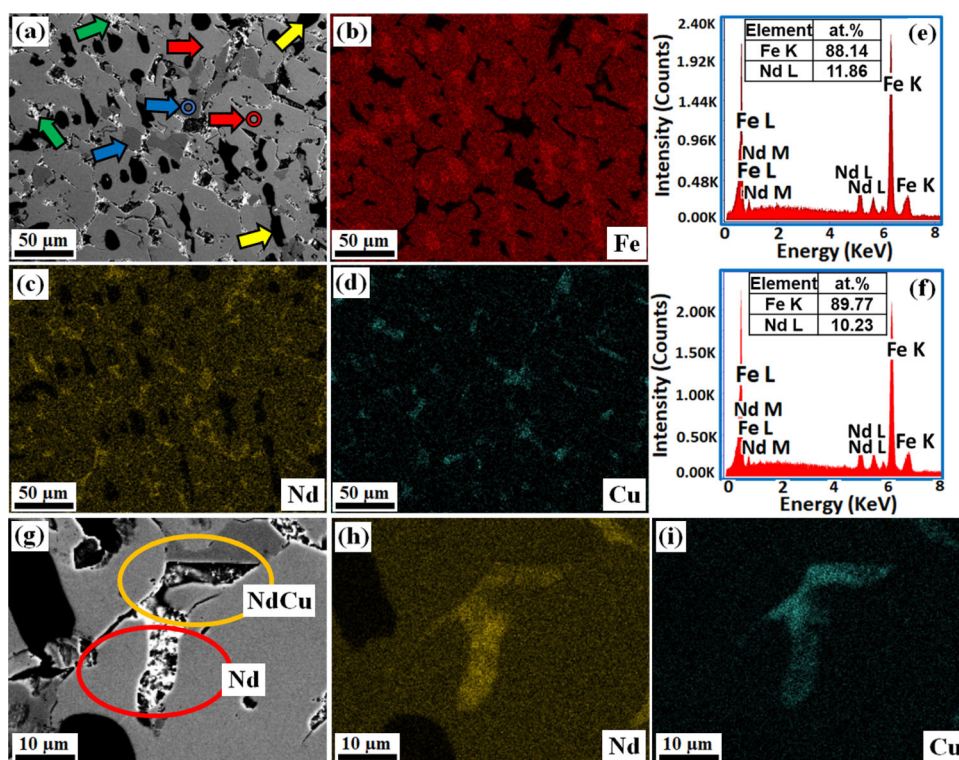


Fig. 3. (a) BSE micrograph of the AC alloy and (b–d) EDS elemental distribution maps showing distribution of (b) Fe, (c) Nd, and (d) Cu; (e–f) point EDS analysis of the (e) light gray region (encircled by red) and (f) dark gray region (encircled by blue); (g) BSE micrograph of the Nd-rich region and (h–i) EDS elemental distribution of (h) Nd and (i) Cu (Color figure online).

Table II. Phase fraction values in the AC microstructure

Phases	Phase fraction (in %)
Primary-Fe	12 ± 0.8
Nd ₂ Fe ₁₇	7.5 ± 0.3
Nd-rich	9 ± 0.5
Nd ₂ Fe ₁₄ B	Balance

starts decreasing from ~ 1420 K. As γ -Fe decreases, evolution of Nd₂Fe₁₄B and Nd₂Fe₁₇ phases takes place at ~ 1413 K. The amount of Nd₂Fe₁₄B increases to ~ 80 wt.% with continued cooling and remains more or less constant till the cooling completes. Simultaneously, several complex phase transformations result in formation of Nd₅Fe₁₇, NdCu, and Nd-rich phase with decrease in temperature. To mimic the phase evolution under actual casting conditions, the non-equilibrium Scheil-Gulliver model is employed. The Scheil-Gulliver cooling calculations are performed using the developed thermodynamic database, and the results are outlined in Fig. 4b. Correspondingly, a Scheil-Gulliver cooling plot depicting the compositional change in the liquid phase during solidification is presented in Fig. 4c. As evident from the Scheil-Gulliver cooling calculations in Fig. 4b, the γ -Fe phase is first to nucleate from the liquid phase, hereafter referred to

as primary-Fe. In the Scheil-Gulliver calculations, the amount of primary-Fe increases till 30 wt.% between 1560 K and 1418.92 K. With further decrease in temperature, the γ -Fe phase fraction remains constant at 30 wt.%. The Nd₂Fe₁₇ phase is formed in the temperature range between 1418.92 K and 1412.32 K, and its phase fraction also remains unchanged with further decrease in temperature. This observation suggests that as the alloy undergoes solidification, the liquid phase traverses through the phase fields of primary Fe and Nd₂Fe₁₇. Consequently, the amount of these phases remains constant with further decrease in temperature. Figure 4b further shows that formation of the Nd₂Fe₁₄B phase from liquid takes place at ~ 1412.32 K. In the temperature range between 1326.57 K and 886.65 K, Nd₂Fe₁₄B and Nd_{1.1}Fe₄B₄ co-precipitate from the liquid phase, which is evident from the increase in their phase fraction as observed in Fig. 4b. As illustrated in Fig. 4c, in the temperature range of 1412.32 K to 886.65 K, the Fe in the liquid phase is continuously decreasing while B and Cu are relatively constant. Consequently, the liquid composition shifts to Nd-rich part of the quaternary system where Nd and Nd₅Fe₁₇ phases are formed at 886.65 K and 873.97 K, respectively. The solidification terminates at the final eutectic temperature (766.11 K) with the formation of β -NdCu and Nd as eutectic components. This observation is further confirmed in the EDS elemental

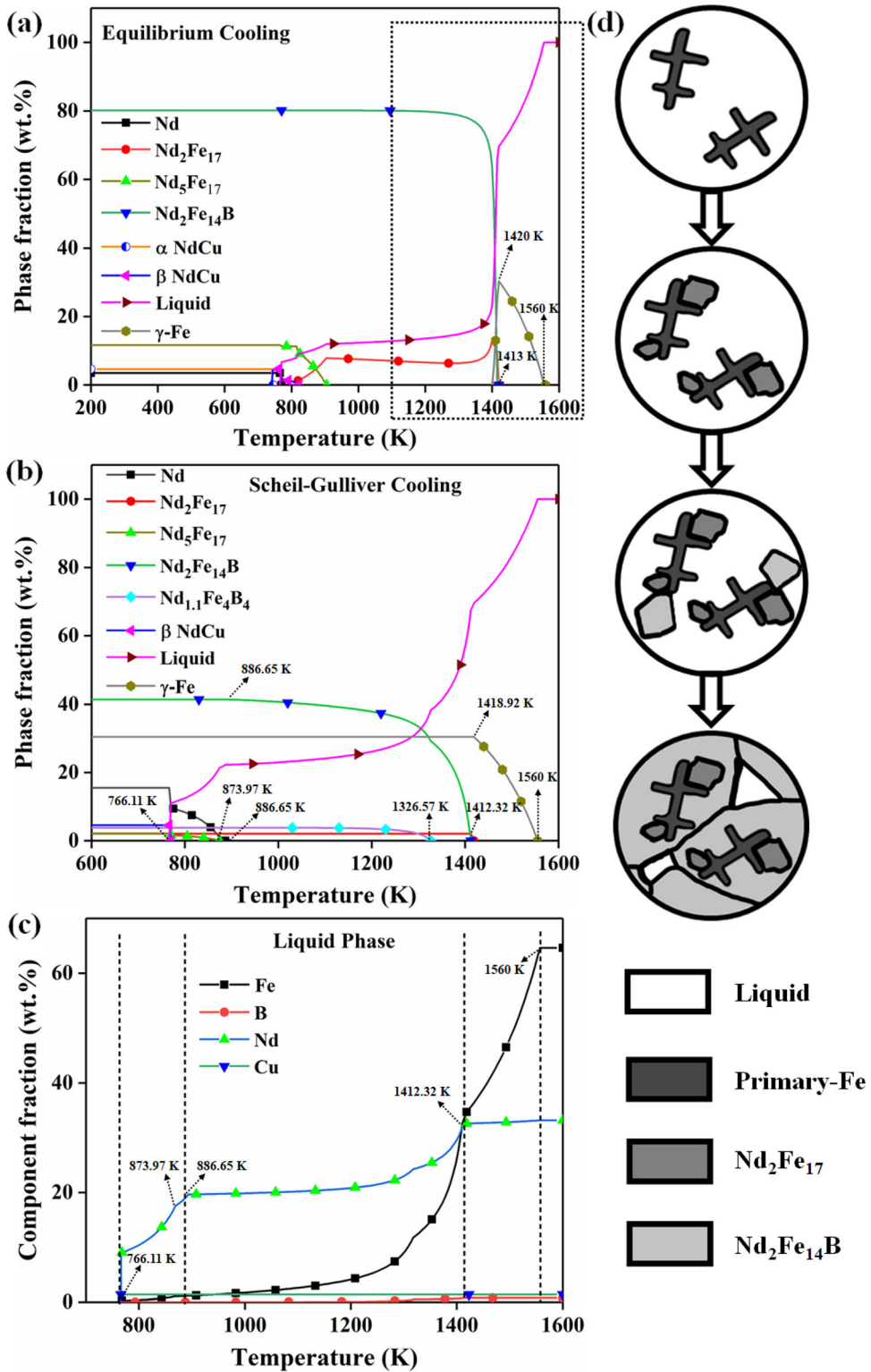


Fig. 4. (a) Equilibrium and (b) Scheil-Gulliver cooling plot of the AC alloy; (c) compositional change in the liquid phase during cooling of the liquid as per the Scheil-Gulliver cooling calculations; (d) schematic illustration showing the solidification sequence leading towards the formation of $Nd_2Fe_{14}B$ phase in the AC alloy.

maps of Nd and Cu in Fig. 3h and i, respectively, where the Nd and NdCu eutectic components are observed at the inter-dendritic regions in the AC microstructure. The Scheil-Gulliver calculations suggest the formation of a core-shell-type structure, wherein the primary-Fe dendrites comprise the core, surrounded by $\text{Nd}_2\text{Fe}_{17}$ and the matrix $\text{Nd}_2\text{Fe}_{14}\text{B}$ phase, as observed in Fig. 3a. The remnant primary-Fe undergoes allotropic transformation from γ -Fe (FCC) into α -Fe (BCC) without any morphological change in the parent phase. However, this allotropic transformation from γ -Fe (FCC) to α -Fe (BCC) is not observed in the Scheil-Gulliver cooling calculations in Fig. 4b. This is primarily because the solidification begins at the γ -Fe (FCC) phase field and the liquid composition continuously shifts to the Nd-rich part of the quaternary system without ever crossing the α -Fe (BCC) phase field. The overall solidification sequence leading to the formation of $\text{Nd}_2\text{Fe}_{14}\text{B}$ phase is schematically shown in Fig. 4d. Phases such as $\text{Nd}_{11}\text{Fe}_4\text{B}_4$ and $\text{Nd}_5\text{Fe}_{17}$, as depicted in the Scheil calculations in Fig. 4b, are not observed in the microstructure of

the AC alloy possibly because of their low content in this condition.

Effect of Homogenization Treatment

To reduce the debilitating effect of primary-Fe, it is desirable to minimize the presence of the detrimental primary-Fe phase through a homogenization treatment. An enlarged view of the selected region of the equilibrium cooling plot (refer Fig. 4a) is represented in Fig. 5a. A systematic analysis influencing the selection of the homogenization temperature is carried out with the help of equilibrium cooling plot and the DSC plot (Fig. 5b). As explained in section 3.2, formation of $\text{Nd}_2\text{Fe}_{14}\text{B}$ begins at ~ 1413 K (indicated as T_p in Fig. 5a) along with decrease in primary-Fe. Furthermore, the DSC plot of the AC alloy in Fig. 5b shows the onset of an endothermic peak at ~ 1413 K, indicating melting of the $\text{Nd}_2\text{Fe}_{14}\text{B}$ phase during heating of the alloy. Ensuring that the $\text{Nd}_2\text{Fe}_{14}\text{B}$ phase does not melt during the heat treatment, a homogenization temperature (T_H) of 1373 K prior to the onset of melting of the $\text{Nd}_2\text{Fe}_{14}\text{B}$ phase is selected.

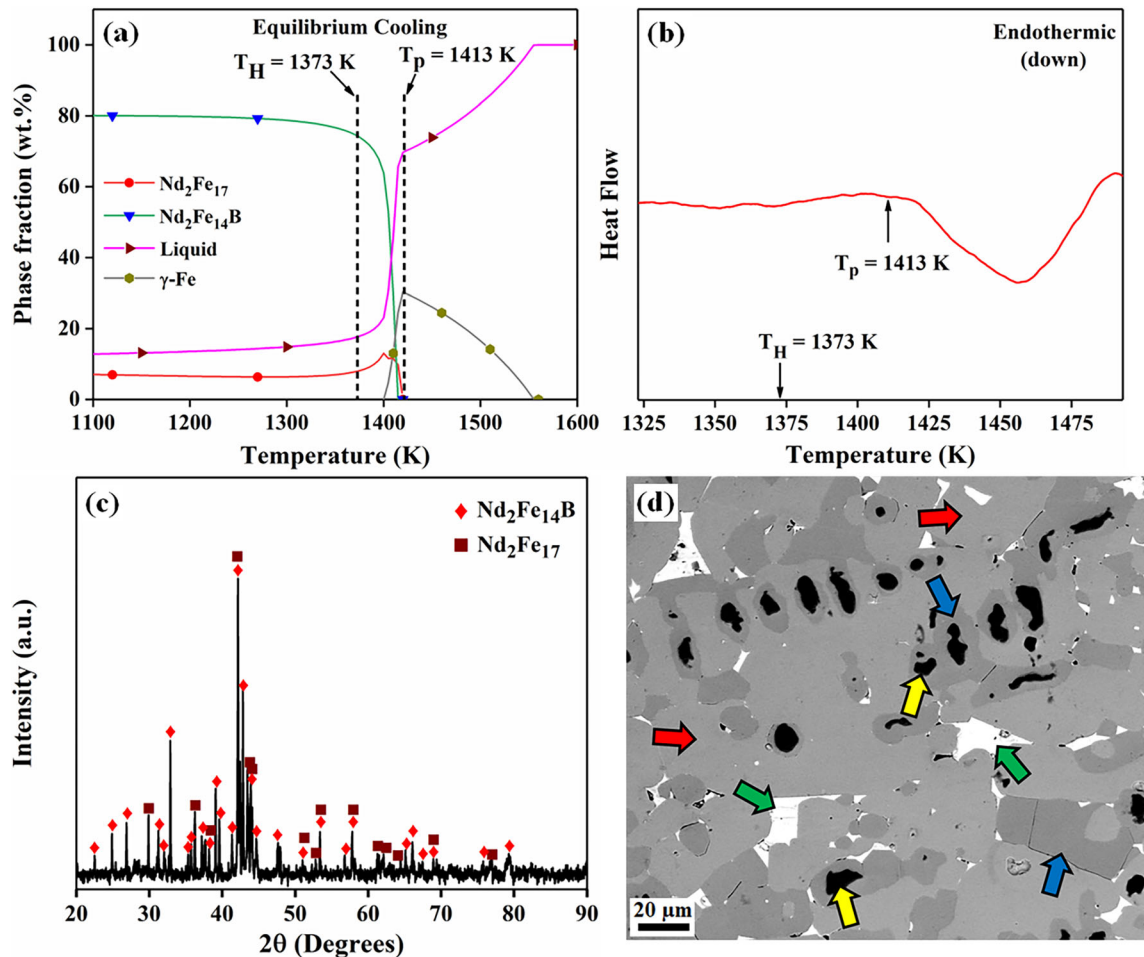


Fig. 5. (a) Equilibrium phase diagram (marked region in Fig. 4a is enlarged) and (b) DSC plot of AC alloy; (c) XRD pattern and (d) BSE micrograph of the AH alloy. The red, blue, yellow, and green arrows in (d) indicate the $\text{Nd}_2\text{Fe}_{14}\text{B}$, $\text{Nd}_2\text{Fe}_{17}$, primary-Fe and Nd-rich phase, respectively (Color figure online).

The XRD pattern and BSE micrograph of the AH specimen are shown in Fig. 5c and d, respectively. The XRD analyses indicates the presence of peaks corresponding to $\text{Nd}_2\text{Fe}_{14}\text{B}$ and $\text{Nd}_2\text{Fe}_{17}$. Distinct XRD peaks corresponding to $\text{Nd}_2\text{Fe}_{17}$ are observed in the XRD pattern of the AH alloy. ICDD PDF number #04-004-4987 is used as a reference to identify the peaks corresponding to the $\text{Nd}_2\text{Fe}_{17}$ phase. The BSE micrograph of the AH alloy reveals presence of $\text{Nd}_2\text{Fe}_{14}\text{B}$ (indicated with red arrow), primary-Fe (indicated with yellow arrow), $\text{Nd}_2\text{Fe}_{17}$ (indicated with blue arrow), and Nd-rich phase (indicated with green arrow). Average phase fraction values of the phases identified in the AH microstructure are presented in Table III. Approximately 70% reduction in the phase fraction of primary-Fe is observed after homogenization. Furthermore, the Nd-rich phase is also reduced by 44% after homogenization, and it is observed mainly at the triple junction regions. Also, a clear phase boundary delineating the individual $\text{Nd}_2\text{Fe}_{14}\text{B}$ grains is not observed in the AH microstructure (Fig. 5d). Nonetheless, it is evident that the size of the $\text{Nd}_2\text{Fe}_{14}\text{B}$ phase in the AH microstructure is relatively coarser compared to that observed in the AC condition, indicating coarsening of the $\text{Nd}_2\text{Fe}_{14}\text{B}$ phase after the homogenization treatment.

Melting and solidification of the Nd-Fe-B-Cu alloy as well as the homogenization treatment results in evolution of complex microstructures due to the line compound nature of the $\text{Nd}_2\text{Fe}_{14}\text{B}$ matrix phase. The resulting microstructures in both AC and AH alloy exhibit many undesirable features, including non-optimal size of matrix $\text{Nd}_2\text{Fe}_{14}\text{B}$ crystallites, heterogeneous distribution of Nd-rich intergranular phases, and presence of soft magnetic primary-Fe and $\text{Nd}_2\text{Fe}_{17}$ phases. The evolution of the soft magnetic phases in the Nd-Fe-B-Cu alloy microstructure reduces the amount of desirable hard magnetic $\text{Nd}_2\text{Fe}_{14}\text{B}$ phase. Their existence in the microstructure shunts the magnetic field, thus reducing the hard magnetic properties of the alloy.²⁷ In addition, the reduction in primary-Fe phase fraction after homogenization treatment is accompanied by an increase in the $\text{Nd}_2\text{Fe}_{17}$ phase, which is also soft magnetic in nature and not desirable. It is also understood that presence of primary-Fe in the conventional AC microstructure is unavoidable and can be suppressed through

Table III. Phase fraction values in the AH microstructure

Phases	Phase fraction (in %)
Primary-Fe	3.6 ± 0.8
$\text{Nd}_2\text{Fe}_{17}$	23.2 ± 0.6
Nd-rich	5 ± 0.5
$\text{Nd}_2\text{Fe}_{14}\text{B}$	Balance

direct/congruent solidification of the $\text{Nd}_2\text{Fe}_{14}\text{B}$ phase by rapid solidification processing routes.¹¹

CONCLUSION

In this work, the solidification sequence of a Nd-Fe-B-Cu alloy composition is investigated to unravel the post-solidification microstructure under non-equilibrium cooling conditions. Furthermore, the effect of a homogenization treatment on the evolution of microstructure, especially dissolution of the remnant primary-Fe, is studied. In this context, the following conclusions are drawn from the investigation:

- The XRD and SEM-EDS analyses collectively indicate that the $\text{Nd}_{15.5}\text{Fe}_{78}\text{B}_5\text{Cu}_{1.5}$ alloy contains primary-Fe, $\text{Nd}_2\text{Fe}_{14}\text{B}$, Nd-rich phase (Nd/NdCu eutectic), and $\text{Nd}_2\text{Fe}_{17}$ phases in the AC microstructure. The Scheil-Gulliver cooling calculations can effectively explain the microstructure evolution in the AC alloy.
- The retainment of primary-Fe in the AC microstructure leading to a core-shell-type structure is explained appropriately with the help of Scheil-Gulliver cooling calculation.
- A significant reduction in the phase fraction of primary-Fe is achieved after the homogenization treatment. In addition, significant grain coarsening of the $\text{Nd}_2\text{Fe}_{14}\text{B}$ phase is also observed in the AH microstructure.

ACKNOWLEDGEMENTS

The funding received from DRDO (ER&IPR) for this work is gratefully acknowledged.

CONFLICT OF INTEREST

On behalf of all authors, the corresponding author states that there is no conflict of interest.

REFERENCES

1. O. Gutfleisch, M.A. Willard, E. Brück, C.H. Chen, S.G. Sankar, and J.P. Liu, *Adv. Mater.* 23, 821 (2011).
2. K. Hono and H. Sepehri-Amin, *Scr. Mater.* 67, 530 (2012).
3. K. Hono and H. Sepehri-Amin, *Scr. Mater.* 154, 277–283 (2018).
4. S. Sugimoto, *J. Phys. D Appl. Phys. D: Appl. Phys.* 44, 064001 (2011).
5. O. Tosoni, E.B. Mendonça, J. Reijonen, A. Antikainen, L. Schäfer, S. Riegg, and O. Gutfleisch, *Addit. Manuf. Manuf.* 64, 103426 (2023).
6. F. Chen, *J. Magn. Magn. Mater. Magn. Mater.* 514, 167227 (2020).
7. Y. Liu, X. Liao, J. He, H. Yu, X. Zhong, Q. Zhou, and Z. Liu, *J. Magn. Magn. Mater. Magn. Mater.* 504, 166685 (2020).
8. Y. Tang, Y. Li, X. Xu, M. Yue, W. Liu, H. Zhang, Q. Lu, and W. Xia, *J. Mater. Sci. Technol. Mater. Sci. Technol.* 80, 28 (2021).
9. L. Schäfer, K. Skokov, F. Maccari, I. Radulov, D. Koch, A. Mazilkin, E. Adabifroozjaei, L. Molina-luna, and O. Gutfleisch, *Adv. Funct. Mater. Funct. Mater.* 33, 2208821 (2022).
10. J.J. Croat, *Rapidly Solidified Neodymium-Iron-Boron Permanent Magnets* (Woodhead Publishing, Duxford, 2018).

11. J. Cui, J. Ormerod, D. Parker, R. Ott, A. Palasyuk, S. Mccall, M.P. Paranthaman, M.S. Kesler, M.A. McGuire, I.C. Nlebedim, C. Pan, and T. Lograsso, *JOM* 74, 1279 (2022).
12. C. Tan, Q. Wei, W. Cheng, X. Liu, Y. Bai, and J. Wang, *Materials* 16, 4697 (2023).
13. D. Su, K.C. Yang, M.H. Rong, X. Cheng, Q. Wei, Q.R. Yao, J. Wang, G.H. Rao, and H.Y. Zhou, *Mater. Res Express.* 7, 106513 (2020).
14. J. Gao, T. Volkmann, S. Roth, W. Löser, and D.M. Herlach, *J. Magn. Magn. Mater. Magn. Magn. Mater.* 234, 313 (2001).
15. W.C. Chang, T.S. Chin, and K.S. Liu, *J. Magn. Magn. Mater. Magn. Magn. Mater.* 80, 352 (1989).
16. M. Reichel, P. Groche, O. Gutfleisch, and J. Schröder, *Proc. Appl. Math. Mech. Appl. Math. Mech.* 23, e202300104 (2023).
17. R. Caniou, C. Rado, G.C. Gaillard, O. Tosoni, C. Flament, and J.P. Garandet, *J. Magn. Magn. Mater. Magn. Magn. Mater.* 570, 170503 (2023).
18. D.W. Scott, B.M. Ma, Y.L. Liang, and C.O. Bounds, *J. Appl. Phys.* 79, 4830 (1996).
19. C.W. Bale, E. Bélisle, P. Chartrand, S.A. Deckerov, G. Eriksson, A.E. Gheribi, K. Hack, I.H. Jung, Y.B. Kang, J. Melançon, A.D. Pelton, S. Petersen, C. Robelin, J. Sangster, P. Spencer, and M.A. Van Ende, *Calphad* 55, 1 (2016).
20. M.A. Van Ende and I.H. Jung, *J. Alloys Compd. Alloys Compd.* 548, 133 (2013).
21. A. Hussain, M.A. Van Ende, J. Kim, and I.H. Jung, *Calphad* 41, 26 (2013).
22. P. Wang, L. Zhou, Y. Du, H. Xu, S. Liu, L. Chen, and Y. Ouyang, *J. Alloys Compd. Alloys Compd.* 509, 2679 (2011).
23. C.P. Wang, S.H. Guo, A.T. Tang, F.S. Pan, X.J. Liu, and K. Ishida, *J. Alloys Compd. Alloys Compd.* 482, 67 (2009).
24. K. Shubhank and Y.B. Kang, *Calphad* 45, 127 (2014).
25. V. Sofronov, A. Buinovskiy, Y. Makaseev, E. Kartashov, I. Rusakov, and A.I.P. Conf, *Proc.* 1772, 030002 (2016).
26. M.B. Siva Kumar, D. Prabhu, M. Sadhasivam, B. Manjusha, N. Chandrasekaran, K.G. Pradeep, G. Sundararajan, and R. Gopalan, *Mater. Res. Lett.* 10, 780 (2022).
27. N. Sridharan, E. Cakmak, F.A. List, H. Ucar, S. Constantinides, S.S. Babu, S.K. McCall, and M.P. Paranthaman, *J. Mater. Sci. Mater. Sci.* 53, 8619 (2018).

Publisher's Note Springer Nature remains neutral with regard to jurisdictional claims in published maps and institutional affiliations.

Springer Nature or its licensor (e.g. a society or other partner) holds exclusive rights to this article under a publishing agreement with the author(s) or other rightsholder(s); author self-archiving of the accepted manuscript version of this article is solely governed by the terms of such publishing agreement and applicable law.